

Juno-UVS Observation of the Io Footprint During Solar Eclipse

Key Points:

- Juno-UVS observed for the first time the Io footprints while Io went into eclipse
- The effect of Io's atmospheric collapse on the footprint emitted power is investigated
- No significant variation of the footprint emitted power is observed during eclipse

Supporting Information:

- Supporting Information S1
- Table S1
- Figure S1
- Figure S2
- Figure S3
- Figure S4

Correspondence to:

V. Hue,
vhue@swri.org

Citation:

Hue, V., Greathouse, T. K., Bonfond, B., Saur, J., Gladstone, G. R., Roth, L., et al. (2019). Juno-UVS observation of the Io footprint during solar eclipse. *Journal of Geophysical Research: Space Physics*, 124, 5184–5199. <https://doi.org/10.1029/2018JA026431>

Received 3 JAN 2019

Accepted 20 MAY 2019

Published online 11 JUL 2019

V. Hue¹, T. K. Greathouse¹, B. Bonfond², J. Saur³, G. R. Gladstone^{1,4}, L. Roth⁵, M. W. Davis¹, J.-C. Gérard², D. C. Grodent², J. A. Kammer¹, J. R. Szalay⁶, M. H. Versteeg¹, S. J. Bolton¹, J. E. P. Connerney^{7,8}, S. M. Levin⁹, P. C. Hinton^{1,10}, and F. Bagenal^{1,10}

¹Southwest Research Institute, San Antonio, TX, USA, ²STAR Institute, LPAP, Université de Liège, Liège, Belgium,

³Institut für Geophysik und Meteorologie, Universität zu Köln, Cologne, Germany, ⁴Department of Physics and Astronomy, University of Texas at San Antonio, San Antonio, TX, USA, ⁵School of Electrical Engineering, Royal Institute of Technology KTH, Stockholm, Sweden, ⁶Department of Astrophysical Sciences, Princeton University, Princeton, NJ, USA, ⁷Space Research Corporation, Annapolis, MD, USA, ⁸NASA Goddard Spaceflight Center, Greenbelt, MD, USA, ⁹Jet Propulsion Laboratory, Pasadena, CA, USA, ¹⁰Laboratory for Atmosphere and Space Physics, University of Colorado Boulder, Boulder, CO, USA

Abstract The two main ultraviolet-signatures resulting from the Io-magnetosphere interaction are the local auroras on Io's atmosphere, and the Io footprints on Jupiter. We study here how Io's daily eclipses affect the footprint. Previous observations showed that its atmosphere collapses in eclipse. While remote observers can observe Io's local auroras briefly when Io disappears behind Jupiter, Juno is able to follow the Io footprint in the unlit hemisphere. Theoretical models of the variability of the energy flux into the Alfvén wings, ultimately powering the footprints, are not sufficiently constrained by observations. For the first time, we use observations of Io's footprint from the Ultraviolet Spectrograph (UVS) on Juno recorded as Io went into eclipse. We benchmark the trend of the footprint brightness using observations by UVS taken over Io's complete orbit and find that the footprint emitted power variation with Jupiter's rotation shows fairly consistent trends with previous observations. Two exploitable data sets provided measurements when Io was simultaneously in eclipse. No statistically significant changes were recorded as Io left and moved into eclipse, respectively, suggesting either that (i) Io's atmospheric densities within and outside eclipse are large enough to produce a saturated plasma interaction, that is, in the saturated state, changes in Io's atmospheric properties to first order do not control the total Alfvénic energy flux, (ii) the atmospheric collapse during the Juno observations was less than previously observed, or (iii) additional processes of the Alfvén wings in addition to the Poynting flux generated at Io control the footprint luminosity.

1. Introduction

The tidal heating of Io, caused by Jupiter's proximity and the orbital resonances with Europa and Ganymede (Peale et al., 1979), maintains the most prominent volcanic activity in the solar system. About 1 ton/s of SO₂ escapes from Io's atmosphere (e.g., Thomas et al., 2004). Jupiter possesses the strongest planetary magnetic field in the entire solar system. The Galilean satellites are embedded within Jupiter's strong planetary magnetic field and interact strongly with it. Io, with its SO₂-dominated atmosphere (Morabito et al., 1979; Pearl et al., 1979), plays a crucial role in the magnetosphere of Jupiter. A fraction of the SO₂ escaping Io is dissociated, ionized, and brought to corotation with the Jovian magnetic field. The plasma is then transported outward, forming the plasma sheet (Thomas et al., 2004).

The Galilean satellites act as planetary-sized obstacles to the fast-rotating plasma sheet. Their orbital velocities are lower than the azimuthal velocity of the rotating plasma. The moons are therefore subject to a flow of magnetized plasma, which disturbs the plasma flow in the direction of their orbital motion (Kivelson et al., 2004). In addition to that, the ~10° tilt of the Jovian magnetic dipole moment with respect to Jupiter's rotation axis adds a wobbling effect of the plasma sheet on the Galilean satellites. Several parameters control the characteristics of the plasma flow disturbance produced by the satellites; the relative velocity of the flow with respect to the satellites, their internal properties (intrinsic magnetic field and inductive response

of a conductive layer to time-varying external field) as well as their external properties (atmosphere and ionosphere; e.g., Jia et al., 2010; Saur et al., 2004, 2013).

The strong plasma interaction at Io was revealed when this satellite was first found to control Jupiter decimeter emission (Bigg, 1964). Io's electrodynamic interaction with the plasma flow was found to be responsible for Io's local auroras (e.g., Roesler et al., 1999) as well as the Io footprints (IFPs) and its tail on Jupiter (Connerney et al., 1993). Io's local auroras are generated through the excitation of sulfur dioxide lines as well as OI and SI lines by electron impact (Geissler et al., 1999; Roesler et al., 1999). These emissions are localized in the equatorial region, on its flank with respect to the incoming plasma torus, and oscillate along with the magnetic field (Retherford et al., 2000; Roth et al., 2011; Saur et al., 2000). Io's local auroras and the IFPs both originate from the plasma being diverted around Io. A modification of Io's ionospheric properties is expected to affect the electrodynamic interaction, through a modification of its Pedersen and Hall conductances (Saur et al., 2004, 2013).

The atmosphere of Io has been historically challenging to characterize (Lellouch et al., 2007, and references therein). Despite the lack of doubt regarding the source of Io's atmospheric SO₂, the different observing techniques used to probe its patchy and highly spatially variable atmosphere led to rather diverging results at times (Lellouch et al., 2007). The most recent observations, however, converge toward the conclusion that Io's equatorial dayside atmosphere is sublimation supported (Jessup & Spencer, 2015; Lellouch et al., 2015). The nature of Io's atmosphere, sublimation driven or volcanically supported, can be tested and challenged when observing Io during one of its ~2-hr-long eclipses every orbit of Io. Tsang et al. (2015) did not detect post eclipse change in absorption by SO₂ at near-ultraviolet (NUV) wavelengths. Yet infrared (IR) observations of Io going into eclipse by Tsang et al. (2016) revealed changes in the SO₂ absorption, consistent with a drop of the SO₂ column density by a factor of 5.

The effect of Io's eclipses on its local auroras was previously studied by Clarke et al. (1994) and Saur and Strobel (2004). Io's far-UV (FUV) emissions are affected by the amount of neutrals. As the amount of neutrals increases, the number of ion-neutral collisions leading to Io's local auroras also increases. Saur and Strobel (2004) modeled Io's FUV emissions during eclipse for different ratios of volcanically to sublimation-driven components of Io's atmosphere. When the modeled volcanic contribution is greater than a few percent of the sublimation component, Io's FUV emissions are predicted to increase during eclipse. As the volcanic contribution decreased, the emitted FUV radiation were found to drop past ingress and brighten at egress. Previous observing campaigns observed Io's auroras during eclipse and showed a dimming and brightening of the atomic emission lines around ingress and egress, respectively (Clarke et al., 1994; Retherford et al., 2007; Roth et al., 2011; Trafton et al., 2012). This was attributed to a decrease in sulfur dioxide column density during eclipse through condensation. However, the persistence of Io's auroras during eclipse still suggests a nonnegligible contribution from volcanism (Geissle et al., 2004; Roth et al., 2014).

The focus of the present paper is to study the effect of a change in Io's atmospheric properties on Io's electrodynamic interaction. While previous studies focused on Io's local auroras, we investigate the change in Io's electrodynamic interaction on its footprints. The opportunity provided by Juno's unique vantage point in the Jovian system allows such observations for the first time.

The Io auroral footprint is a manifestation of a strong electrodynamic interaction, in which plasma is slowed down and diverted in the vicinity of Io. This generates a perturbed electric field in Io's conducting atmosphere, driving ionospheric currents. At a certain distance from Io, the ionospheric conductivities are not high enough to maintain currents perpendicular to the magnetic field, so currents continue along the magnetic field direction to feed the Alfvén wings region of the interaction through Alfvén waves (Acuna et al., 1981; Belcher et al., 1981; Saur et al., 2004). These waves propagate along the magnetic field lines to both the northern and southern hemispheres of Jupiter. While traveling, they may experience filamentation (Chust et al., 2005) and partial reflections on the plasma density gradients (Goertz, 1980; Neubauer, 1980), if there is a strong enough plasma density gradient. Observations show a rich structure characterized by several spots and tail (e.g., Bonfond et al., 2008; Connerney et al., 1993; Connerney & Satoh, 2000; Clarke et al., 2002; Gérard et al., 2006; Mura et al., 2018), which may be related to reflection or refraction of the Alfvén waves as they travel between Io and the Jupiter's ionosphere.

The main possible processes controlling the morphology and brightness of the footprint spots and tail are as follows:

- the local interaction at Io, which controls the magnetic energy fluxes feeding the Alfvén wings region; this interaction depends on the plasma torus density and, therefore, on the location of Io inside the torus, the velocity at Io, as well as the magnetic field strength (Hess et al., 2010, 2013; Saur et al., 2013);
- the partial reflections of the Alfvén waves at the torus boundaries (Crary & Bagenal, 1997; Gurnett & Goertz, 1981; Jacobsen et al., 2007);
- the electron acceleration mechanism, which depends on the magnetic field topology in the acceleration region (Hess et al., 2010); and
- the possible mirroring of the electrons between the acceleration region and Jupiter’s atmosphere (Hess et al., 2013).

All these quantities vary over a planetary rotation, as Io oscillates around the center of the torus. Previous observations of the IFP performed with the Space Telescope Imaging Spectrograph and the Advanced Camera for Surveys on the Hubble Space Telescope (HST) monitored the evolution of the brightness and emitted power of the footprint as a function of planetary rotation (Bonfond et al., 2013; Gérard et al., 2006; Wannawichian et al., 2010). The key finding was that Io’s footprints become brighter when located near the denser center of the torus, that is, when Io is located at SIII W-longitude (λ_{III} hereafter) of $\sim 110^\circ$ and 290° .

Since the aforementioned processes modulate the electrodynamic interaction, they need to be considered in order to isolate the eclipse contribution. Data recorded by the UVS on the Juno mission (Juno-UVS) were used to achieve this goal. In the first section, we present the Juno-UVS instrument, the observations performed, and the data reduction methodology. We compare the results with previous observations, as well as theoretical considerations. We then present the specific observations performed during eclipse and extract the eclipse contribution from the natural modulation of the footprint. Finally, the physical interpretation and conclusion are presented.

2. Observation of the Io Footprint

2.1. The Juno-UVS Instrument

Juno-UVS is a photon-counting spectrograph covering the spectral range 68–210 nm and designed to target most of the UV emissions produced in Jupiter’s auroral regions (Gladstone et al., 2017). This includes the H₂ bands (Werner, Lyman and Rydberg), as well as the Lyman- α series. Juno-UVS successfully provided the first views on the nightside Jovian auroras (Bonfond et al., 2017; Gérard et al., 2018), provided new constraints on the vertical distribution of Io’s footprint tail emissions (Szalay et al., 2018), and has monitored the overall auroral activity during approach (Gladstone et al., 2017). It has also made regular observation of the sky during cruise, used to characterize the instrument (Greathouse et al., 2013). Since then, the characterization was extended for the rest of the cruise and the Jupiter operations (Hue et al., 2019).

The instrument borrows heavily from previous UVS instruments by Southwest Research Institute (SwRI); the Rosetta’s and New Horizon’s Alices, as well as the Lunar and Reconnaissance Orbiter-Lyman-Alpha Mapper Project (LRO-LAMP). The main differences are (i) an improved shielding, (ii) an improved microchannel plate readout scheme ($2,048 \times 256$), (iii) a dog-bone-shaped slit, composed of two wide segments ($2.55^\circ \times 0.2^\circ$ each), and a narrow segment ($2^\circ \times 0.025^\circ$), and (iv) a scan mirror, designed to bring flexibility in the instrument pointing. The instrument spectral resolution varies along the slit from 1.3 nm (at the center of the slit) up to 3 nm (Greathouse et al., 2013).

Juno nominally spins at 2 rpm, and UVS’ nominal field of view is looking radially outward from Juno’s spin axis. Over a ~ 30 -s spacecraft rotation period, UVS observes a $\sim 7.2^\circ \times 360^\circ$ swath of the sky, with ~ 17 ms integration time in the wide slit, and ~ 2 ms in the narrow slit. The boundaries between both wide and the narrow slits are 0.05° long. The addition of the scan mirror allows targeting up to $\pm 30^\circ$ away from the spin plane, giving the opportunity to access half the sky at any moment by combining the rotation of the spacecraft and the mirror pointing flexibility. When the scan mirror is rotated by an angle ϕ with respect to UVS’ nominal field of view, the sky-projected slit is rotated therefore increasing the effective exposure time on any observed point source. Since changing the mirror position implies two rotations of the sky-projected slit, the integration time scales up as $\cos^2\phi$, when the scan mirror is rotated by an angle ϕ (see Supporting Information S1).

The UVS perijove (PJ) observations usually run from -5 to $+5$ hr with respect to each PJ, with a variable temporal coverage, as UVS is turned off during the radiation belt crossing to avoid excessive radiation levels. During a PJ observation, Juno’s distance to Jupiter center ranges from $7 R_J$ down to $1.05 R_J$ at PJ. The spa-

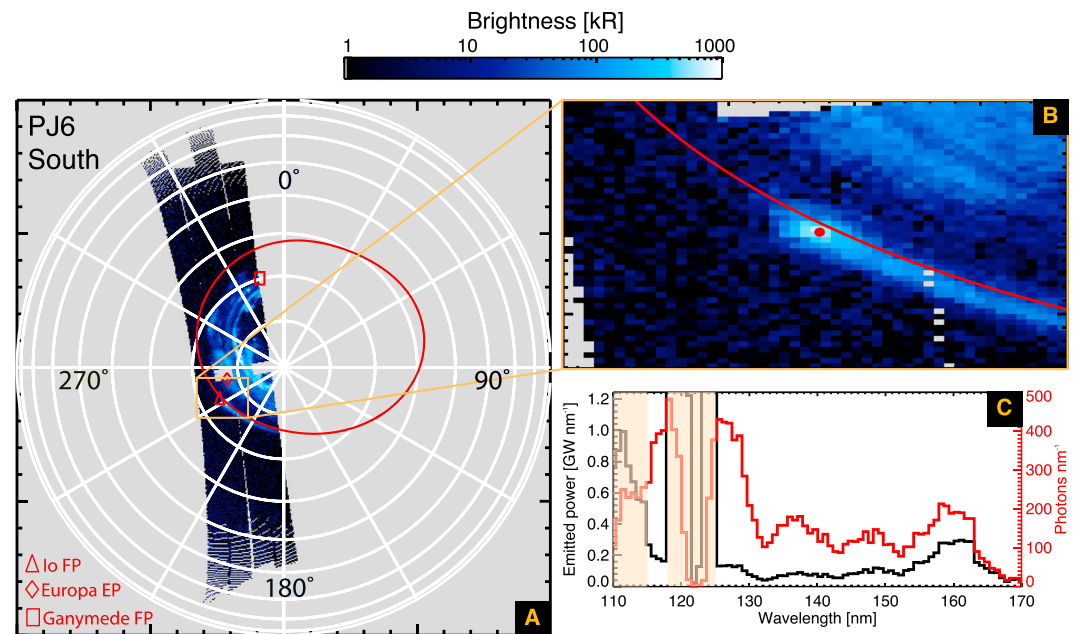


Figure 1. Typical Io footprint observation from five coadded swaths of ultraviolet spectrograph data. (a) Polar projection over the south pole showing the coadded swaths. The red solid line denotes the surface location of the path traced out by the Io footprint as Jupiter rotates (Bonfond et al., 2017). The various symbols display the expected positions of the satellite footprint, mapped to the surface along field lines using the JRM09 model of the planetary magnetic field (Connerney et al., 2018) in combination with a model magnetodisc (Connerney et al., 1981). (b) Zoom over the Io footprint. The red solid line displays the previously observed footprint path. The red circle denotes the centroid of the observed footprint emission. (c) Integrated emitted power and photon counts from the footprint. The black line shows the emitted power integrated over a large fraction of the Io footprint (see section 2.2), while the red line shows the photon count from that same region.

tial resolution of UVS on the planet therefore evolves substantially, since the angular size of Jupiter as seen by Juno ranges from 15° up to 150° . As Juno gets closer, UVS only gets a narrow swath of Jupiter's aurora each spin, and numerous scan mirror pointings are needed to cover the entire auroras. It typically takes ~ 40 spins (20 min) to produce a full image of Jupiter's auroras at a range of $1.6 R_J$. During a PJ observation sequence, gaps in the IFP observation coverage are due to (i) UVS looking at other sections of the aurora, or (ii) Juno being within Jupiter's high-radiation regions, leading to limited to no data recorded (e.g., Kammer et al., 2018). Additionally, some regions of the IFP located in UVS' swath might be missing, due to a buffer-speed limitation occurring when observing extended and bright UV emissions. To mitigate this effect, several swaths of data, recorded successively, were coadded in order to build up signal as well as increase the spatial coverage over the footprint.

Typical observations of the IFP are presented on Figure 1, where five consecutive swaths of data were coadded. The details for each coadded swath are provided on Table 1. Figure 1 includes an overview plot over the southern aurora, as well as a zoom over the IFP. The gray-shaded region of the images correspond to places where no data were recorded by UVS. Isolated gray pixels were often observed as a consequence of data gap on several swaths. The quoted brightnesses correspond to the integrated brightness from 115–118 nm and 125–165 nm, and multiplied by 1.84 to extrapolate the brightness over the total $H_2 + Lyman-\alpha$ emissions, from 75–198 nm, using a H_2 synthetic spectrum from Gustin et al. (2013). At wavelengths shorter than 115 nm and in the 118–125-nm range, displayed as shaded boxes, the calibration of the instrument is not reliable yet.

2.2. Emitted Power of the Footprint

Due to the highly variable observing geometry of the UVS observations, a sophisticated retrieval method was developed to consistently calculate the emitted power of the footprint. This method makes the use of the surface location of the path traced out by the IFP as Jupiter rotates previously published by Bonfond et al. (2017), hereafter denoted as footprint path. The main challenge lies in the changing spatial resolution of UVS over the footprint. The width of the IFP, that is, perpendicular to the footprint path, is first unresolved

Table 1
Details of the Coadded Swaths Used to Produce Figure 1

Spin #	Time (UTC)	Time rel. to PJ	Altitude	λ_{III} (Io)	Io local time (hr)
1	07:16:48	+1.27 hr	1.59 R_J	228.9°	13.68
2	07:17:18	+1.28 hr	1.61 R_J	229.1°	13.69
3	07:17:49	+1.28 hr	1.62 R_J	229.3°	13.69
4	07:18:19	+1.29 hr	1.63 R_J	229.6°	13.70
5	07:18:49	+1.30 hr	1.64 R_J	229.8°	13.70

Note. The set of swath was recorded during the PJ6 sequence on 19 May 2017 and the displayed times correspond to the ultraviolet spectrograph nadir-pointed times during which each swath was recorded. Additional relevant information includes the time relative to PJ, the altitude of the spacecraft, as well as the S3 W-longitude (λ_{III}) and local time of Io. PJ = perijove; FP = footprint.

and progressively becomes resolved, as Juno gets closer to the planet. Unless UVS resolves the IFP the entire time, in which case the peak brightness would be meaningful, the brightness should otherwise be handled with care (Bonfond et al., 2013), and the emitted power should be preferred to using the brightnesses.

The close-up views allow UVS to resolve the different auroral spots, with a limited coverage over the entire footprint and tail emission. The distant observations, on the other hand, provide more contextual views of the entire footprint and tail but does not allow one to spatially separate the different spots. Only the overall emitted power of the footprint can be derived from these views.

In order to compare on a similar baseline between the close-up views and the distant ones, the approach taken in this work is to derive the overall emitted power of the IFP by consistently integrating over the same spatial region over the planet. The footprint path published by Bonfond et al. (2017) was used to compute the distances of every pixel across and along that path, with respect to the position of the brightest spot, corresponding to the Main Alfvén Wing (MAW) spot. The superposition of these contours on the zoomed views over the IFP (Figure 1b) is presented on Figure 2.

To compute the overall IFP emitted power, the flux from the footprint was integrated up to $\pm 2,300$ km perpendicular to the footprint path (i.e., equatorward and poleward), 4,000 km upstream (i.e., opposite to the tail

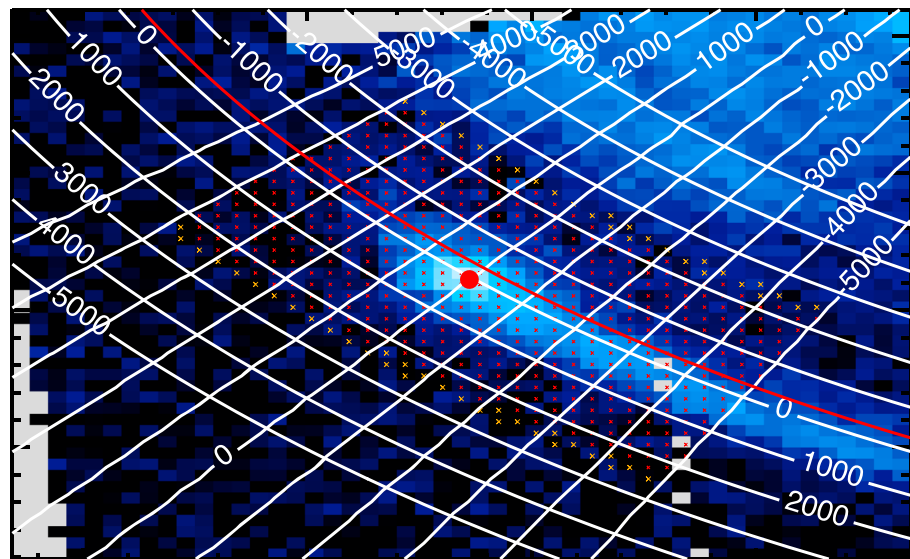


Figure 2. Zoom over the Io footprint observation from Figure 1b. The distances of every pixel across and along the footprint path are overlaid. One set of contour displays the distances (km) of each pixel in the direction parallel to the footprint path (negative is taken toward the pole). The other set of contour shows the distances along the footprint path, starting from the centroid of the footprint emission (red dot), and taken negative downstream of the footprint tail. The red crosses show the integration region for the emitted power calculation of the footprint and the orange crosses show two boundaries used to remove the diffuse background ultraviolet emission.

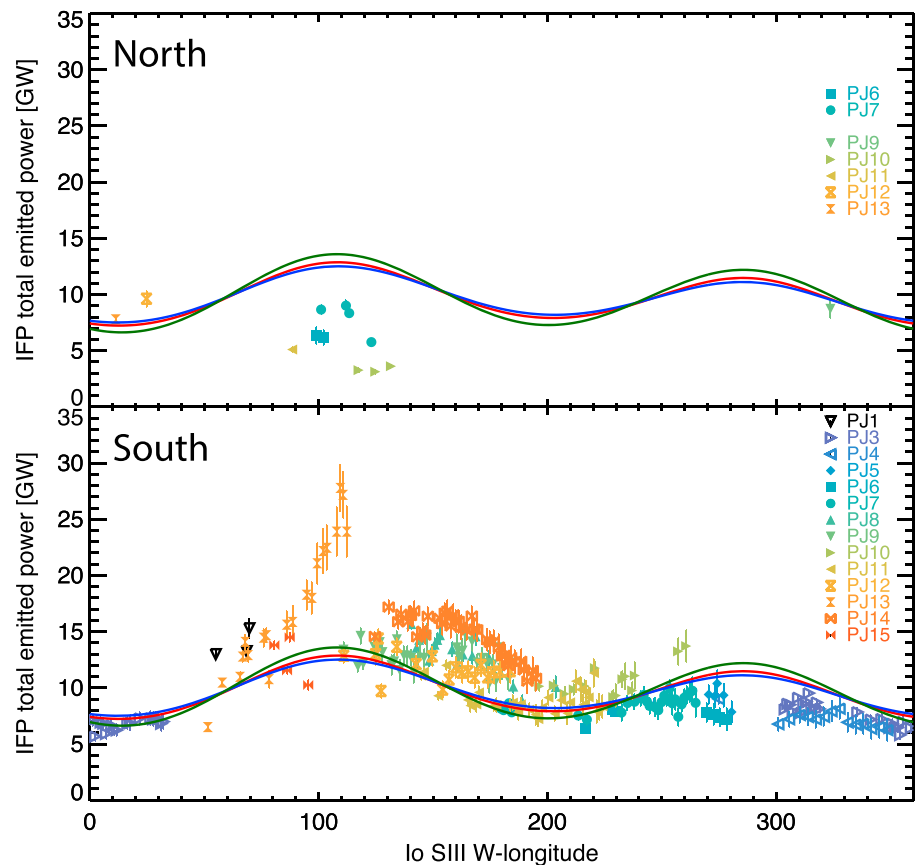


Figure 3. Emitted power of the northern Io footprint (top) and southern Io footprint (bottom). The theoretical variation of the Poynting flux is overplotted using the JRM09 magnetic field model and using different models of Io's Pedersen conductance (see section 2.3 and Figure 4).

direction), and 5,000 km down the tail. The choice of the integration region was defined such that it includes all the secondary spots near the MAW spot. The size of that region affects the emitted power retrieval, as it accounts for a variable amount of tail emission. Reducing the integration region by $\pm 2,000$ km perpendicular to the footprint path, 3,000 km upstream, and 3,000 km down the tail reduces the retrieved emitted power by less than 8%, without however changing the relative differences between the several sets of data. The resulting integration region is displayed on Figure 2 as red crosses.

Sources of noise in the power from the footprint arise from (i) the high-radiation environment; (ii) reflected sunlight from Jupiter; and (iii) the diffuse background UV emission from Jupiter's auroral region. The data have been subtracted for the background radiation. The method employed to perform the background radiation subtraction consisted in using the counts recorded in the obstructed, yet active, part of the detector located at short wavelengths. The recorded photon counts are then subtracted such that the number of detections in that part of the detector is offset to zero, and a relative estimate of the effective area is then used to calculate the correction to apply at longer wavelengths. In order to limit the amount of reflected sunlight, only the counts measured up to 165 nm have been included in the power calculation. The diffuse background UV emission, both caused by the reflected sunlight and Jupiter's diffuse auroras, was subtracted from the emitted power calculation. The Jovian diffuse auroral emissions equatorward of the main oval are thought to be produced from energetic electron pitch angle scattering from whistler mode waves (e.g., Bhattacharya et al., 2001, 2005; Li et al., 2017; Radioti et al., 2009). The diffuse background UV emission was subtracted by fitting a linear baseline on both sides of the spatial integration region. We have made sure that the same trends were obtained after the background subtraction when reducing the integration band pass down to

140 nm, in order to minimize even more the contribution from the reflected sunlight (see supporting information). The boundary regions used for the diffuse background subtraction are shown as orange crosses on Figure 2. The uncertainty on the derived power comes from the shot noise uncertainty.

The emitted power (EP) of the footprint was calculated following

$$EP = f \times \sum_{\lambda} \frac{hc}{\lambda} 4\pi d^2 \sum_{x,y} \frac{C_{x,y}^{\lambda} \times \Omega_{x,y}}{t_{x,y}} \cos \theta_{x,y}, \quad (1)$$

where $\sum_{x,y}$ represents the summation over the selected footprint emission region, $C_{x,y}^{\lambda}$ is the number of counts in a wavelength bin λ corrected for the deadtime effects of UVS, d is the Juno-IFP distance, $t_{x,y}$ is the integration time of each pixel, and $\theta_{x,y}$ is the emission angle, used to perform a first-order correction for the limb brightening effect. The parameter $\Omega_{x,y}$ represents the solid angle of the (x,y) pixel used to bin the recorded counts. Finally, h , c , and λ are Planck's constant, the speed of light, and the wavelength. The total power measured in the 115- to 118-nm and 125- to 165-nm band pass is then scaled by $f = 2.04$ to extrapolate the power over the total H₂+ Lyman- α emissions, from 75–198 nm, using a H₂ synthetic spectrum from Gustin et al. (2013).

The EP retrieved from all the IFP data is shown on Figure 3, presented as a function of λ_{III} . The top and bottom panels, respectively, show the northern and southern footprints EP. The theoretical EP variation (see section 2.3) is presented and rescaled to fit the measured EP.

HST observations showed that the southern IFP brightness and EP is enhanced near Io's plasma sheet crossings, around $\lambda_{III} \sim 110^\circ$ and at $\lambda_{III} \sim 290^\circ$. This double-peak feature was previously found to be asymmetric, with the $\lambda_{III} = 110^\circ$ crossing being ~ 1.4 times brighter than the $\lambda_{III} = 290^\circ$ one (Bonfond et al., 2013; Wannawichian et al., 2010). The enhancement at the $\lambda_{III} = 290^\circ$ crossing was not measured by UVS, although more PJ passes will be needed to conclude on this. The increase in the EP at $\lambda_{III} = 110^\circ$ was measured to be ~ 3 times higher than the EP measured at $\lambda_{III} = 200^\circ$, making it broadly consistent with previous results of Bonfond et al. (2013), despite their lack of repeated measurements in the $\lambda_{III} \sim 110^\circ$ sector.

The northern IFP was observed by HST in the $\lambda_{III} = 110\text{--}280^\circ$ range. The observation of UVS over the northern IFP is sparser than that in the south. This is partially due to the characteristics of the Juno orbit, which causes UVS to experience more radiation during the northern passes as the mission advances. Here we report measurements mostly in the $\lambda_{III} = 0\text{--}30^\circ$ and $90\text{--}130^\circ$ ranges. The limited overlap of the λ_{III} coverage with previous studies makes difficult any comparative study. The focus of this study will therefore be on the southern IFP.

2.3. Theoretical Consideration

The Poynting flux S quantifies the amount of energy radiated away due to the electrodynamic interaction (Saur et al., 2013):

$$S = 2\pi R_{\text{eff}}^2 \frac{(\bar{\alpha} M_A B_0)^2}{\mu_0} v_A, \quad (2)$$

where R_{eff} is the radius of the interaction region, taken here as $1.3 \times R_{\text{Io}}$ to account for the extension of the atmosphere-ionosphere (Kivelson et al., 2004). M_A is the Alfvén mach number, B_0 the strength of the magnetic field, v_A the Alfvén speed velocity, μ_0 the permeability of free space, and $\bar{\alpha}$ the strength of the interaction (Saur & Strobel, 2004; Saur et al., 2013). The parameter $\bar{\alpha}$ depends on the Pedersen and Alfvén conductances, Σ_P and Σ_A , respectively (Neubauer, 1998; Saur et al., 1999), such that

$$\bar{\alpha} = \frac{\Sigma_P}{\Sigma_P + 2\Sigma_A}. \quad (3)$$

Io's Pedersen conductance corresponds to the summation of the local Pedersen conductivities, integrated along the magnetic field line. It cannot be directly measured and has to be modeled (e.g., Kivelson et al., 2004; Saur et al., 1999). An averaged Pedersen conductance of $\Sigma_{P,0} = 200$ Siemens (Kivelson et al., 2004) was used here. Following Saur et al. (2013), we use a scaling of Io's Pedersen conductance by the plasma density surrounding Io, $\Sigma_P = (n/n_0)^x \Sigma_{P,0}$, as well as the torus model of Bagenal and Delamere (2011). This is used here as a first approximation in the framework of the model of Saur et al. (2013) focusing on the

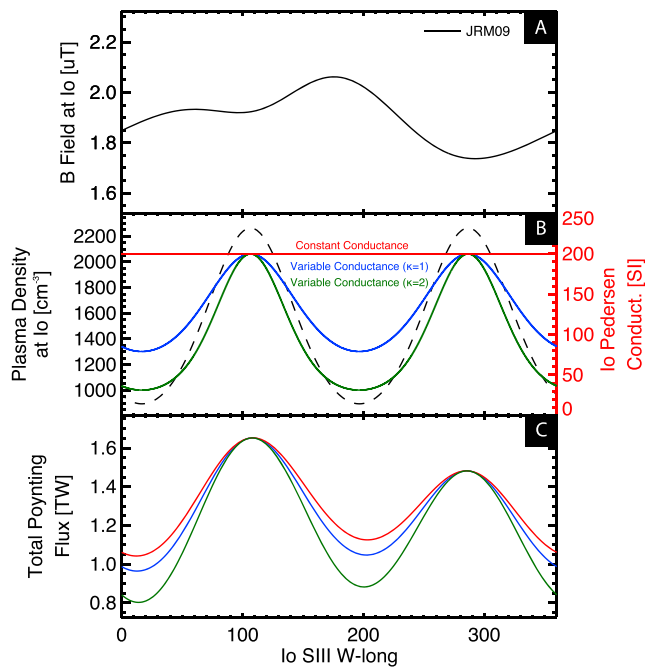


Figure 4. (a) Evolution of the magnetic field strength at Io as a function of Io's SIII W-longitude using the JRM09 model. (b) Evolution of the density at Io (black, left-hand-side axis), from the torus model of Bagenal and Delamere (2011). The right-hand-side axis denotes the evolution of the Pedersen conductance for different values of κ : $\kappa = 0$ (red), $\kappa = 1$ (blue), $\kappa = 2$ (green), following Saur et al. (2013). (c) Evolution of the Poynting flux generated by the interaction at Io from equation (2) and using the different values of the conductance. The line color displays the type of Pedersen conductance model used.

electrodynamic interaction only. A physical chemistry model simulating multispecies, coupled with a MHD model of the local interaction at Io, such as the one presented by Dols et al. (2008, 2012), would be required to further quantify the detailed aspects of the atmospheric collapse effect on the local interaction electrodynamic. Executing such task, which is poorly constrained at the time of the eclipse observations, is beyond the scope of this work. The goal of this paper is to assess the effect of the collapse on the footprint EP from the observational point of view, based on the current knowledge of the footprint emission processes.

Figure 4 shows the evolution of the Poynting flux generated in the region of interaction around Io using the recent field model based on Juno magnetometer data, JRM09 (Connerney et al., 2018). It was then associated with the “CAN” current sheet model (Connerney et al., 1981). Several scalings of the Pedersen conductance were used ($\kappa = 0$, $\kappa = 1$, $\kappa = 2$), following Saur et al. (2013). According to this Poynting flux model, while the variation in the magnetic field is mostly responsible for the asymmetry in the strength of the interaction at the two plasma sheet crossings, the modulation of Io's Pedersen conductance increases the amplitude variations of the EP over a planetary rotation. Most of the theoretical models used here do not reproduce the single-peak trend observed in the footprint EP. However, we stress again that the model of the Poynting flux is not expected to accurately describe the observed variability, because additional processes also play a role, as discussed in section 1.

2.4. Power Variation as a Function of Local Time

HST has been monitoring the IFP for a variety of geometry, as the Earth-Jupiter distance varies up to $\sim 25\%$ annually and the emission angle of the northern and southern footprints lies in the $\sim 40\text{--}80^\circ$ range. Juno now gives the opportunity to observe it over a wide range of local times (LT, hereafter) and with various geometry (altitude, emission angle).

Previous observations from Voyager UVS demonstrated the presence of a LT asymmetry in the brightness of the Io torus (Sandel & Broadfoot, 1982). This was later interpreted as the existence of a dawn-dusk electric field either caused by plasma motion flowing down the magnetotail (Barbosa & Kivelson, 1983; Ip & Goertz, 1983), or required by the horizontal closure of field-aligned Birkeland currents (Goertz & Ip, 1984; Murakami et al., 2016). This electric field forces ions to be pushed further away on the dawnside and further in on the duskside. Asymmetry in the structure of the torus may affect the brightness of the IFP. For instance, an asymmetry in the plasma density at Io between the dusk and dawn sides could cause an asymmetry in the footprint brightness, at comparable λ_{III} .

Figure 5 represents the emitted power of the IFP retrieved from the Juno-UVS data, displayed in the LT and λ_{III} space. PJ9 and PJ12 were recorded at almost opposite LTs on the dawnside and duskside, respectively. They both show consistent values for the emitted power. Similarly, PJ6 and PJ7 data set, recorded on both sides of the noon sector show consistent values one another. PJ13 and PJ15 were recorded at LTs somewhat similarly opposite with respect to the noon sector. The beginning of the PJ15 observation shows values in agreement with the PJ13 data, but then start to diverge past λ_{III} of 90° . Finally, PJ14 displays an unusually bright IFP. The power derived on this data set is ~ 4 GW higher than the ones recorded at the similar λ_{III} but very different LTs.

The IFP power retrieved at or near the plasma sheet crossings, that is, during PJ9, PJ12, and PJ13, were recorded at very different LTs and does not show a consistent behavior. The footprint power retrieved during the PJ13 plasma sheet crossing is ~ 15 GW higher than during PJ9 and PJ12. Whether these situations only occur at specific LTs or are controlled by other processes will be investigated in future studies, as more data covering the LT- λ_{III} parameter space will be available.

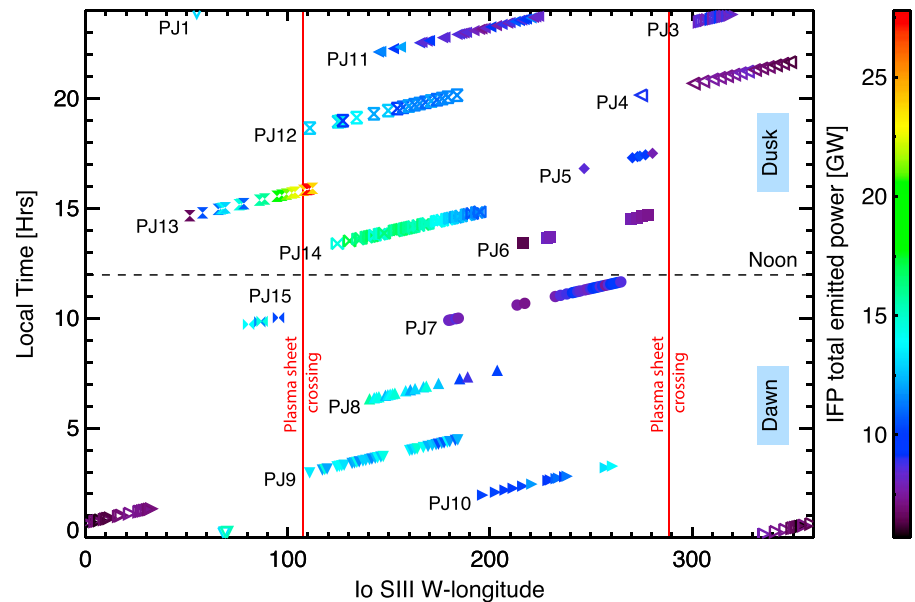


Figure 5. Total emitted power of the southern Io footprint as a function of S3 W-longitude of Io as well as the local time of Io. Each perijove is shown with a different symbol. Once Juno-ultraviolet spectrograph starts to observe the footprint at a given perijove, the λ_{III} and the local time only increase over time. The plasma sheet crossing is displayed with vertical red lines. The noon sector is shown as a dashed line.

3. Modulation of the Electrodynamical Interaction by Io's Atmospheric Collapse

3.1. Eclipse on Io

Io experiences daily eclipses during its 1.76 days orbital period. Once Io enters into Jupiter's umbra, it takes about 4 min before it turns into full eclipse configuration (Tsang et al., 2016). The eclipse then lasts for about 2 hr. Table 2 summarizes the eclipses overlapping with a PJ observation sequence, as of PJ15 (7 September 2018).

UVS operated and provided a large data set during PJ3, PJ9, PJ10, and PJ11. Unfortunately, the IFP data taken on PJ9 and PJ10 were recorded several hours after Io exited Jupiter's umbra. This paper only focuses the simultaneous eclipse observations recorded on PJ3 and PJ11. In the next section, we extract the EP from the footprint over these two data sets and study the potential effect from the atmospheric collapse on the IFP.

3.2. Contribution From the Eclipse on the Footprint Emitted Power

Previous studies by Bonfond et al. (2013), Gérard et al. (2006), and Wannawichian et al. (2010) as well as this work show that the IFP brightness and emitted power may vary significantly with time. Extracting the effect of Io's atmospheric collapse on the EP can be done, for instance, by identifying the general power variation caused by the Io torus wobbling-related density variation.

Table 2

List of the Perijoves (PJ) for Which UVS Has Overlapping or Nearby IFP Observations While Io Was in Eclipse

PJ# and time	Ingress		Egress	
	Time	Io λ_{III}	Time	Io λ_{III}
PJ1 (27 Aug 2016 - 12:50:44)	13:13:18	27.0°	15:26:37	88.7°
PJ3 (11 Dec 2016 - 17:03:41)	13:13:18	296.7°	19:51:39	357.8°
PJ9 (24 Oct 2017 - 17:42:31)	12:48:23	296.5°	19:51:39	356.5°
PJ10 (16 Dec 2017 - 17:56:58)	15:02:05	71.7°	17:11:19	131.4°
PJ11 (7 Feb 2018 - 13:51:49)	17:15:02	206.4°	19:24:05	266.0°

Note. The quoted ingress and egress times correspond to Io's full eclipse configuration.

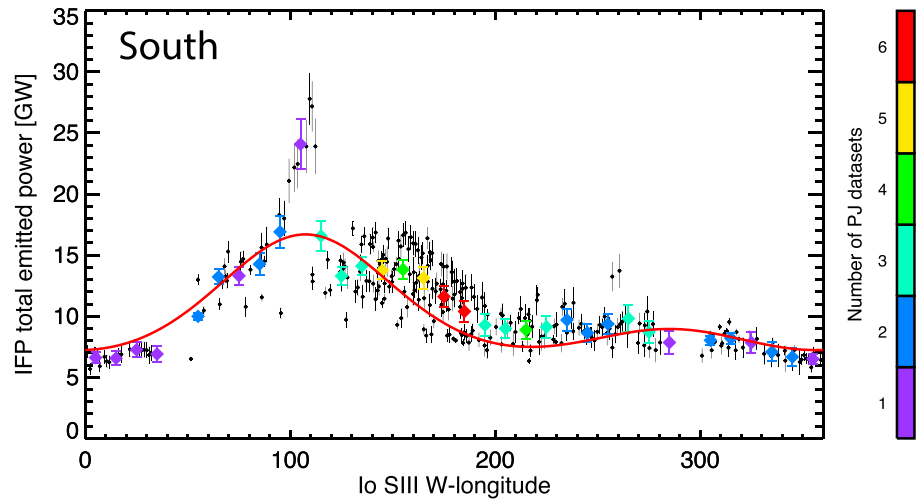


Figure 6. Evolution of the southern Io footprint emitted power from the Juno-UVS measurements as a function of Io's system III W-longitude. Black crosses denote the power measurements. Color coded dots correspond to the binned data, using $\Delta \lambda_{III} = 10^\circ$ bins. The red curve display the best fit function, following the work of Wannawichian et al. (2013).

The Poynting flux models described in section 2.3 are not appropriate to extract the eclipse contribution because they only represent a modest fit of the observation. Due to the lack of stronger constraints on the EP variation with λ_{III} , a data-driven approach has been opted for here. The general power variation of the IFP was extracted by fitting the UVS data available from all the PJs. Because the UVS observations are not evenly distributed in the λ_{III} space, any least squares fit will be dominated by the highly populated region. To remove this bias, we binned the retrieved EP using $\Delta \lambda_{III} = 10^\circ$ bins. Then, the binned data were fitted using a variant of function (5) from Wannawichian et al. (2013). The form of this function is as follows:

$$P(\lambda_{III}) = C_1 \sqrt{\exp\left[-\frac{z^2}{H^2}\right]} \times \left(1 + C_2 \exp\left[-\left(\frac{\lambda_{III} - 110}{\Delta \lambda_1}\right)^2\right]\right), \quad (4)$$

where z represents Io's distance from the centrifugal equator, H the scale height of the torus at Io's distance ($H = 0.75 R_J$, Bagenal & Delamere, 2011), and $\Delta \lambda_1$ represents the typical Gaussian width of the exponential increase seen in the data at $\lambda_{III} = 110^\circ$.

The three parameters (C_1 , C_2 , and $\Delta \lambda_1$) from the function were then adjusted using a Levenberg-Marquardt least squares fitting procedure using IDL's *MPFIT* routine (Markwardt, 2009). The shot-noise uncertainties of the photon counts were used as weight function of the fitting procedure. Figure 6 presents the retrieved EP of the southern IFP, the binned set of data over which the fit was performed, and the fit itself. It also presents the number of the different PJ data sets used to produced the binned data, using a color coding. The $\lambda_{III} = 115\text{--}275^\circ$ sector has been well covered by the UVS. In that sector, we note a particularly important variation in the retrieved EP. Based on previous HST campaign covering a larger period, we expect a similar magnitude in the variability at all observed λ_{III} . Therefore, any fit of the Juno-UVS data series will be slightly biased until the λ_{III} parameter space will be fully explored. The fit presented here is therefore subject to uncertainties and will be used to compare the general trend followed by the IFP.

The eclipse observations recorded during PJ3 and PJ11 are presented in Figure 7, as a function of the Io LT. The shaded area denotes when Io was in eclipse. The red line represents the fit shown on Figure 6 derived from the entire UVS southern footprint data set, up to PJ15. The current λ_{III} of Io and the predicted Alfvén travel time between Io and the southern footprint are shown at the times of ingress and egress. The blue vertical lines indicate the typical timescales over which a change in the electrodynamic interaction would propagate after ingress and egress, based on the Alfvén travel times. The orange vertical lines indicate the typical timescale of 20 min of the collapse of Io's atmosphere (see Figure 3 of Tsang et al., 2016)

The Alfvén travel time was calculated using a 3-D plasma torus model, combined with the JRM09 magnetic field model (Hinton et al., 2019). This information provides a typical timescale over which one would expect

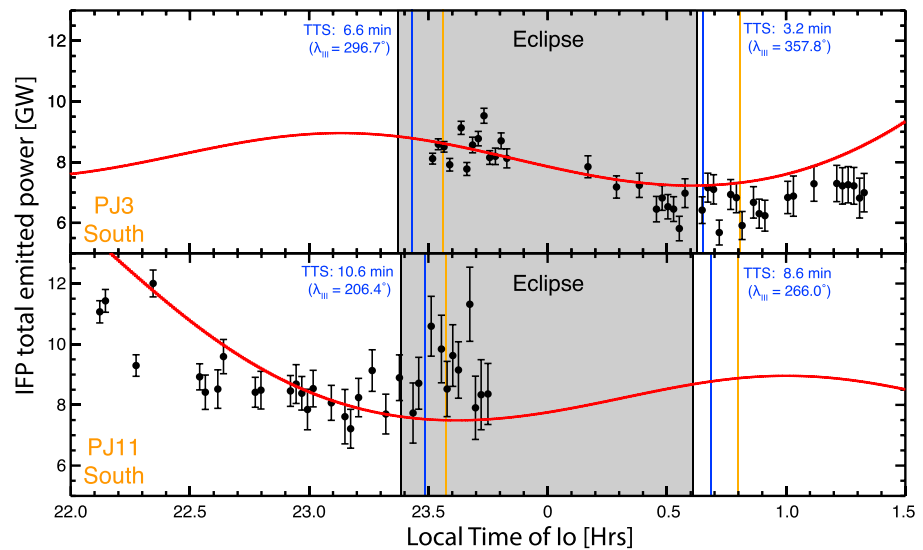


Figure 7. Evolution of the southern Io footprint emitted power measured by ultraviolet spectrograph during the Io eclipses on PJ3 (top panel) and PJ11 (bottom panel), as a function of the local time of Io. The shaded boxes represent the time window during which Io was in eclipse. The blue line represents the Alfvén travel time between Io and Io southern footprint (TTS) both after ingress and egress. The yellow lines denote the typical 20-min timescale over which Io's atmosphere has been observed to collapse. The red curves represent the fit from Figure 6 of the general trend followed by the Io footprint emitted power as a function of Io's longitude.

the information to propagate from Io's region of interaction to Jupiter's ionosphere. Consequently, if Io's atmospheric collapse has an effect on the footprint itself, this effect should be observable from ingress/egress up to 20 min plus the Alfvén travel time to the southern IFP.

The PJ3 data set provided the best coverage of the footprint during eclipse, as of PJ15 (7 September 2018). UVS observed the southern footprint between LT of 23.5 hr up to LT of 1.3 hr, corresponding to 15 min past ingress up until 75 min after egress. The longitude of Io ranged from $\lambda_{III} = 303^\circ$ at ~ 15 min past ingress, up to $\lambda_{III} = 32^\circ$ at the end of the observation sequence. From LT of 23.5 hr (15 min past ingress) up until LT of 23.8 hr (50 min past ingress), the IFP EP increased from 8.4 ± 0.2 GW up to 9.3 ± 0.2 GW, when fitting a linear trend to that time series. At the same time, the overall behavior of the EP as retrieved from a dozen PJs, despite not capturing the stochastic fluctuations of the footprint brightness, predicts instead a decrease from 9.5 to 8.2 GW. At LT of 0.2 hr (84 min past ingress), after a 32 min data gap, the observed EP was 7.8 ± 0.4 GW. It then reached a minimum of 6.5 ± 0.4 GW near egress, and increased again until 7.3 ± 0.6 GW at LT of 1.3 hr (75 min past egress).

The PJ11 data set provided an almost continuous temporal coverage of the footprint during ingress, as the last 38 min of the almost 3-hr-long observations were recorded past ingress. The UVS started to observe the IFP at LT of 22.1 hr (more than 2 hr before ingress). At the beginning of the observation, the EP was measured to decrease from 11.3 ± 0.4 GW, down to 8.2 ± 0.7 GW at LT of 23.1 hr (30 min prior to ingress). The EP then increased throughout ingress up to 9.5 ± 1.0 GW at LT of 23.7 hr (38 min past ingress).

Both PJ3 and PJ11 observations show an increasing signal-to-noise ratio with LT, caused by the increasing distance with time of Juno with respect to the southern footprint. The next section is dedicated to the interpretation of the eclipse observations.

3.3. Physical Interpretation

The observations of the footprint were performed at various stages of the eclipse. The Io footprint observations began when Io was already in eclipse on PJ3 and observed throughout egress, while the PJ11 observations caught the ingress transition.

Theoretical investigations have studied how the state of the electrodynamic interaction at Io and the UV radiation emitted from Io's atmosphere evolve during eclipse (Saur & Strobel, 2004). The main point was that observing how these radiation evolve as Io moves inside and outside of eclipse allows deriving the magnitude of the collapse as well as the importance of the volcanic support with respect to the background atmosphere.

Because of the time delay needed for the electrodynamic interaction to adjust to Io's changing column density, the largest variations in these UV emissions are predicted to occur within 15 min after ingress and over an hour past egress. Using this model, observations with New-Horizons and HST around ingress and egress were best interpreted in the case where volcanoes supply 1% to 3% of Io's dayside atmosphere (Retherford et al., 2007).

Observing the effect of Io's atmospheric collapse on the footprint adds a layer of complexity, since a change in Io's electrodynamic interaction is seen after propagation along the magnetic field lines and through the prism of the additional processes discussed in section 1.

The observed change in the IFP EP at egress during PJ3 is $\Delta EP = 0.7 \pm 0.5$ GW, that is, an increase from 6.6 ± 0.4 GW at LT of 0.5 hr up to 7.3 ± 0.6 GW at LT of 1.2 hr. This lies within the expected change of the footprint EP variation outside of eclipse, that is, an increase from 7.2 GW at LT of 0.5 hr up to 8.1 GW at LT of 1.2 hr, as derived from all the PJ observations up to PJ15. Unfortunately, UVS did not observe the southern footprint prior to ingress, which prevents us from estimating the EP variation at ingress.

During PJ11, the measured EP prior to the eclipse, in the $LT = 23\text{--}23.4$ -hr sector, was 8.2 ± 0.7 GW. An eclipse effect on the EP, if any, should be seen at the time of the eclipse plus the Alfvén travel time, thus at LT of 23.5 hrs and beyond. In the 23.5-23.8 LT sector, the measured EP was 9.3 ± 1.0 GW. No statistically significant changes were therefore recorded, as the measured variation in the EP is within the measurement uncertainties. The apparent increase in the EP over time prior to eclipse, although within the measured uncertainties, seems to contradict the expected change of the footprint EP. It should be reminded that the expected change of the EP is subject to uncertainties, which might not depict the most complete representation of the EP fluctuating behavior as a function of λ_{III} , due to the poor sampling in several λ_{III} sectors.

One explanation of the small variability of the footprint brightness during eclipse is that the electrodynamic interaction at Io is approximately in saturation. In the saturated state, a change in Io's atmospheric properties does not control the total Alfvénic energy flux, at the first order. This means that large enough atmospheric densities outside and inside eclipse produce a nearly saturated plasma interaction at Io. The saturation level of Io's interaction has not been measured/observed quantitatively before. In situ measurements by the Galileo spacecraft were only local and could not directly constrain the overall level of interaction strength and saturation. An alternative explanation for the small change in the footprint brightness during eclipse could be that the atmospheric density decrease during eclipse was relatively small during the time of the observations.

In a simple first step to better understand the variability of the footprint brightness during eclipse, we thus calculate the change in the total Poynting flux of Io's Alfvén wings out of eclipse S_0 and in eclipse S_e

$$\Delta S_{\text{rel}} = \frac{S_0 - S_e}{S_0}. \quad (5)$$

Using the expression for the Poynting flux in (2) (see also Saur et al., 2013) leads to

$$\Delta S_{\text{rel}} = \frac{\bar{\alpha}_0^2 - \bar{\alpha}_e^2}{\bar{\alpha}_0^2}. \quad (6)$$

The interaction strength $\bar{\alpha}$ can be related to a shielding factor alpha through $\alpha = 1 - \bar{\alpha}$. The shielding factor describes how much Io is shielded against the plasma flow with $\alpha = 0$, meaning the plasma flow is zero within Io's ionosphere and the torus plasma is completely deflected around Io, that is, maximum shielding. The shielding factor alpha can be related to the column density after Saur et al. (2003) through (7).

$$\alpha = \alpha_{\text{ref}} \left(\frac{N_{\text{col}}}{N_{\text{ref}}} \right)^\kappa, \quad (7)$$

for the modeled α from Figure 4 of Saur et al. (2003). This expression approximates α for a column density $N_{\text{col}} > N_{\text{ref}} = 1.8 \times 10^{18} \text{ m}^{-2}$ with $\kappa = -0.57$ and $\alpha_{\text{ref}} = 0.75$.

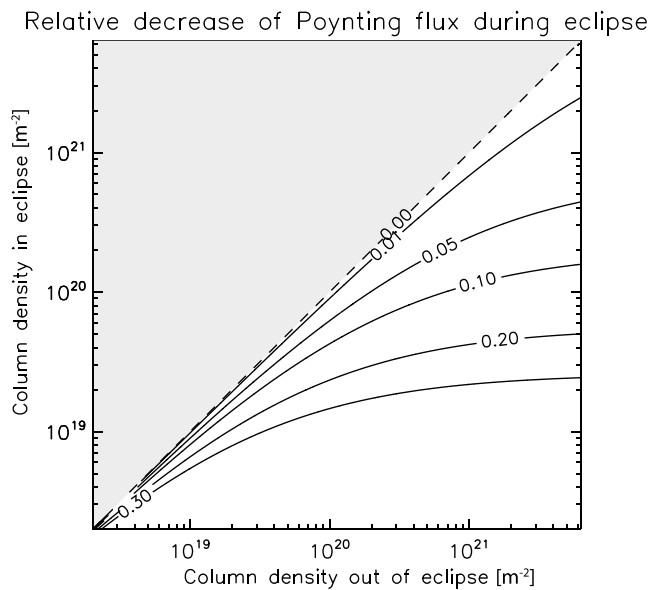


Figure 8. Contour plot showing the relative decrease of Poynting flux when Io enters eclipse. Column densities out of eclipse is on x axis and column density in eclipse on y axis. Gray area is not filled because the column density is not assumed to increase during eclipse.

Using (7) with column densities larger than N_{ref} , we display the relative change of the Poynting flux from (5) as contours in Figure 8. The x axis shows the column density out of eclipse and the y axis show the column density in eclipse. As we assume that the column density does not increase during eclipse we leave the upper left triangle of the figure gray. Figure 8 shows that the relative decrease of the Poynting flux depends nonlinearly on the column densities. The column density of Io's atmosphere outside of eclipse is not tightly constrained. As reviewed by Blöcker et al. (2018) observations of Io's atmosphere indicate that Io's equatorial dayside SO_2 column density ranges from 1×10^{20} to $22 \times 10^{20} \text{ m}^2$ for various heliospheric distances and local times and based on different types of observational techniques (Feaga et al., 2009; Jessup et al., 2004; Jessup & Spencer, 2015; Lellouch et al., 2007; McGrath et al., 2000; Spencer et al., 2005; Tsang et al., 2012). The relative role of Io's sublimation-driven atmosphere compared to its volcanically driven atmosphere, which controls the possible decrease during eclipse, is also not well constrained in the literature.

Looking, for example, at the 0.1 contour in Figure 8, this model predicts a 10% decrease in the Poynting flux when the column densities drop from 10^{21} to 10^{20} m^2 in eclipse. In this case, the interaction could be considered in nearly full saturation. A 10% decrease is also predicted in the case where the column density out of eclipse is 10^{20} m^2 and drops by a factor of ~ 2 in eclipse. The observations presented in this work suggest that the footprint brightness stays relatively constant. If we approximate the uncertainty associated with the Juno-UVS observations presented here by

10%, then the parameter space of atmospheric change during eclipse is constrained to lie within the dashed and the 0.1 contour in Figure 8 based on the simple model presented here.

Another point that needs to be kept in mind is that the Poynting flux fed into the Alfvén wing is only the root energy cause of the footprint, but many other effects such as wave propagation, wave reflection, and the details of the kinetic acceleration processes of the auroral electrons control the footprint emission and are expected to play a role in controlling the UV brightness variability during the eclipse phase.

Previous HST observations suggest that the EP of the different footprint spots are variable over short timescales (Bonfond et al., 2007, 2013). Fluctuations on the order of $\sim 30\%$ are frequently observed for the different Io spots, as well as other footprint (e.g., Bonfond et al., 2017; Grodent et al., 2009). The fluctuations of the different spots are correlated for some λ_{III} sectors, increasing the overall fluctuation of the entire footprint, when the spots are spatially unresolved. The reported timescale for these fluctuations is on the order of 2–5 min and the λ_{III} sector for which the fluctuations of the MAW and the transhemispheric electron beam (TEB) spots are correlated is $78\text{--}99^\circ$. These fluctuations makes the physical interpretation of the Juno-UVS data challenging, since they are on the same order of magnitude, if not greater, than the predicted fluctuations caused by the eclipse.

4. Conclusion

Juno-UVS provides an unprecedented opportunity to study Jupiter's auroral emission from a unique perspective. It allows to study how the emitted power of the IFP evolves as a function of Io's local time. More specifically, UVS observed for the first time the IFP as Io went into eclipse.

The hypothesis challenged in this work is to assess whether UVS measures a notable difference in the footprint emission as Io moves into eclipse. Io's SO_2 dominated atmosphere is tenuous and highly spatially variable. Previous ground-based observation of the Io's atmosphere showed that its surface temperature drops and atmospheric column density collapses within ~ 20 min past eclipse (see Figure 3 of Tsang et al., 2016).

UVS provides snapshots of the footprint every spacecraft rotation (~ 30 s), when UVS is pointing toward it, with typical integration times on the footprint up to ~ 17 ms per spin. Subsequent swaths of UVS data were

coadded in order to increase the signal-to-noise ratio of the observations and fill the frequent coverage gap over the footprint. The emitted power over the entire footprint was derived, since the numerous spots of the footprint cannot be spatially resolved in most distant views from UVS.

The evolution of the southern footprint emitted power is broadly consistent with previous HST observations (Bonfond et al., 2013; Wannawichian et al., 2010), as the data suggest that it peaks at the plasma sheet crossings. Observations of the footprint were recorded at overlapping times with an eclipse in five instances: PJ1, PJ3, PJ9, PJ10, and PJ11. However, only the PJ3 and PJ11 data sets provided exploitable measurements, as they were directly recorded when Io was in eclipse. No statistically significant change was recorded as Io left and entered Jupiter's umbra, respectively.

Theoretical models show that the expected variation of the Poynting flux depend on the partially unconstrained saturation level of Io's interaction (Saur & Strobel, 2004). If Io's electrodynamic interaction strength $\bar{\alpha}$ is close to 1, that is, close to saturation out of eclipse and in eclipse, then only weak changes in the Poynting fluxes are expected. An interaction that is driven out of saturation by a strong decrease due to a collapsing atmosphere can potentially lead to significant variation of the Poynting flux. UVS does not observe a significant change in the Poynting flux variation through the emitted power of the footprints when Io is in eclipse. This suggests that the electrodynamic interaction at Io is approximately in saturation and can be interpreted by the fact that atmospheric densities within and outside of the eclipse are large enough to produce such saturated plasma interaction. Another explanation for the small change through eclipse would be that the magnitude of the atmospheric collapse in eclipse are smaller than the previous observations suggested. Finally, an alternative interpretation could also be that additional properties other than the Poynting flux of the Alfvén wings control the footprint luminosity.

The observation design of UVS, combined with its limited exposure time on the footprint as well as the orbital design of Juno makes it challenging to separate the fluctuations of the footprint from a potential change in Io's atmosphere. Only simultaneous observations of the atmosphere and local emission combined with observations of the footprint would allow one to disentangle these effects.

Acknowledgments

We are grateful to NASA and contributing institutions, which have made the Juno mission possible. This work was funded by NASA's New Frontiers Program for Juno via contract with the Southwest Research Institute. We thank John T. Clarke for useful comments and discussions. B. B., D. C. G., and J.-C. G. acknowledge support from the PRODEX program managed by ESA in collaboration with the Belgian Federal Science Policy Office (BELSPO). The data included herein are either archived or on schedule to be archived in NASA's Planetary Data System (http://pds-atmospheres.nmsu.edu/data_and_services/atmospheres_data/JUNO/juno.html).

References

- Acuna, M. H., Neubauer, F. M., & Ness, N. F. (1981). Standing Alfvén wave current system at Io—Voyager 1 observations. *Journal of Geophysical Research*, *86*, 8513–8521.
- Bagenal, F., & Delamere, P. A. (2011). Flow of mass and energy in the magnetospheres of Jupiter and Saturn. *Journal of Geophysical Research*, *116*, A05209. <https://doi.org/10.1029/2010JA016294>
- Barbosa, D. D., & Kivelson, M. G. (1983). Dawn-dusk electric field asymmetry of the Io plasma torus. *Geophysical Research Letters*, *10*, 210–213.
- Belcher, J. W., Goertz, C. K., Sullivan, J. D., & Acuna, M. H. (1981). Plasma observations of the Alfvén wave generated by Io. *Journal of Geophysical Research*, *86*, 8508–8512.
- Bhattacharya, B., Thorne, R. M., & Williams, D. J. (2001). On the energy source for diffuse Jovian auroral emissivity. *Geophysical Research Letters*, *28*, 2751–2754.
- Bhattacharya, B., Thorne, R. M., Williams, D. J., Khurana, K. K., & Gurnett, D. A. (2005). Diffuse auroral precipitation in the Jovian upper atmosphere and magnetospheric electron flux variability. *Icarus*, *178*, 406–416.
- Bigg, E. K. (1964). Influence of the satellite Io on Jupiter's decametric emission. *Nature*, *203*, 1008–1010.
- Blöcker, A., Saur, J., Roth, L., & Strobel, D. F. (2018). MHD modeling of the plasma interaction with Io's asymmetric atmosphere. *Journal of Geophysical Research: Space Physics*, *123*, 9286–9311. <https://doi.org/10.1029/2018JA025747>
- Bonfond, B., Gérard, J.-C., Grodent, D., & Saur, J. (2007). Ultraviolet Io footprint short timescale dynamics. *Geophysical Research Letters*, *34*, L06201. <https://doi.org/10.1029/2006GL028765>
- Bonfond, B., Gladstone, G. R., Grodent, D., Greathouse, T. K., Versteeg, M. H., Hue, V., et al. (2017). Morphology of the UV aurorae Jupiter during Juno's first perijove observations. *Geophysical Research Letters*, *44*, 4463–4471. <https://doi.org/10.1002/2017GL073114>
- Bonfond, B., Grodent, D., Badman, S. V., Saur, J., Gérard, J.-C., & Radioti, A. (2017). Similarity of the Jovian satellite footprints: Spots multiplicity and dynamics. *Icarus*, *292*, 208–217.
- Bonfond, B., Grodent, D., Gérard, J.-C., Radioti, A., Saur, J., & Jacobsen, S. (2008). UV Io footprint leading spot: A key feature for understanding the UV Io footprint multiplicity? *Geophysical Research Letters*, *35*, L05107. <https://doi.org/10.1029/2007GL032418>
- Bonfond, B., Hess, S., Gérard, J.-C., Grodent, D., Radioti, A., Chantry, V., et al. (2013). Evolution of the Io footprint brightness I: Far-UV observations. *Planetary and Space Science*, *88*, 64–75.
- Bonfond, B., Saur, J., Grodent, D., Badman, S. V., Bisikalo, D., Shematovich, V., et al. (2017). The tails of the satellite auroral footprints at Jupiter. *Journal of Geophysical Research: Space Physics*, *122*, 7985–7996. <https://doi.org/10.1002/2017JA024370>
- Chust, T., Roux, A., Kurth, W. S., Gurnett, D. A., Kivelson, M. G., & Khurana, K. K. (2005). Are Io's Alfvén wings filamented? Galileo observations. *Planetary and Space Science*, *53*, 395–412.
- Clarke, J. T., Ajello, J., Ballester, G., Ben Jaffel, L., Connerney, J., Gérard, J.-C., et al. (2002). Ultraviolet emissions from the magnetic footprints of Io, Ganymede and Europa on Jupiter. *Nature*, *415*, 997–1000.
- Clarke, J. T., Ajello, J., Luhmann, J., Schneider, N., & Kanik, I. (1994). Hubble space telescope UV spectral observations of Io passing into eclipse. *Journal of Geophysical Research*, *99*, 8387–8402.

- Connerney, J. E. P., Acuna, M. H., & Ness, N. F. (1981). Modeling the Jovian current sheet and inner magnetosphere. *Journal of Geophysical Research*, *86*, 8370–8384.
- Connerney, J. E. P., Baron, R., Satoh, T., & Owen, T. (1993). Images of excited H₃⁺ at the foot of the Io flux tube in Jupiter's atmosphere. *Science*, *262*, 1035–1038.
- Connerney, J. E. P., Kotsiaros, S., Oliverson, R. J., Espley, J. R., Joergensen, J. L., Joergensen, P. S., et al. (2018). A new model of Jupiter's magnetic field from Juno's first nine orbits. *Geophysical Research Letters*, *45*, 2590–2596. <https://doi.org/10.1002/2018GL077312>
- Connerney, J. E. P., & Satoh, T. (2000). The H₃⁺ ion: A remote diagnostic of the Jovian magnetosphere, in *Astronomy, physics and chemistry of H₃⁺*. *Philosophical Transactions of the Royal Society of London Series A*, *358*, 2359–2559. <https://doi.org/10.1098/rsta.2000.0661>
- Crary, F. J., & Bagenal, F. (1997). Coupling the plasma interaction at Io to Jupiter. *Geophysical Research Letters*, *24*, 2135.
- Dols, V., Delamere, P. A., & Bagenal, F. (2008). A multispecies chemistry model of Io's local interaction with the plasma torus. *Journal of Geophysical Research*, *113*, A09208. <https://doi.org/10.1029/2007JA012805>
- Dols, V., Delamere, P. A., Bagenal, F., Kurth, W. S., & Paterson, W. R. (2012). Asymmetry of Io's outer atmosphere: Constraints from five Galileo flybys. *Journal of Geophysical Research*, *117*, E10010. <https://doi.org/10.1029/2012JE004076>
- Feaga, L. M., McGrath, M., & Feldman, P. D. (2009). Io's dayside SO₂ atmosphere. *Icarus*, *201*, 570–584.
- Geissle, P., McEwen, A., Porco, C., Strobel, D., Saur, J., Ajello, J., & West, R. (2004). Cassini observations of Io's visible aurora. *Icarus*, *172*, 127–140.
- Geissler, P. E., McEwen, A. S., Ip, W., Belton, M. J. S., Johnson, T. V., Smyth, W. H., & Ingersoll, A. P. (1999). Galileo imaging of atmospheric emissions from Io. *Science*, *285*, 870–874.
- Gérard, J.-C., Mura, A., Bonfond, B., Gladstone, G. R., Adriani, A., Hue, V., et al. (2018). Concurrent ultraviolet and infrared observations of the north Jovian aurora during Juno's first perijove. *Icarus*, *312*, 145–156.
- Gérard, J.-C., Saglam, A., Grodent, D., & Clarke, J. T. (2006). Morphology of the ultraviolet Io footprint emission and its control by Io's location. *Journal of Geophysical Research*, *111*, A04202. <https://doi.org/10.1029/2005JA011327>
- Gladstone, G. R., Persyn, S. C., Eterno, J. S., Walther, B. C., Slater, D. C., Davis, M. W., et al. (2017). The ultraviolet spectrograph on NASA's Juno mission. *Space Science Reviews*, *213*, 447–473.
- Gladstone, G. R., Versteeg, M. H., Greathouse, T. K., Hue, V., Davis, M. W., Gérard, J.-C., et al. (2017). Juno-UVS approach observations of Jupiter's auroras. *Geophysical Research Letters*, *44*, 7668–7675. <https://doi.org/10.1002/2017GL073377>
- Goertz, C. K. (1980). Io's interaction with the plasma torus. *Journal of Geophysical Research*, *85*, 2949–2956.
- Goertz, C. K., & Ip, W.-H. (1984). A dawn-to-dusk electric field in the Jovian magnetosphere. *Planetary and Space Science*, *32*(2), 179–185.
- Greathouse, T. K., Gladstone, G. R., Davis, M. W., Slater, D. C., Versteeg, M. H., Persson, K. B., et al. (2013). Performance results from in-flight commissioning of the Juno ultraviolet spectrograph (Juno-UVS). Uv, x-ray, and gamma-ray space instrumentation for astronomy xviii, Proceedings Society of Photographic Instrumentation Engineers vol. 8859 p. 88590T.
- Grodent, D., Bonfond, B., Radioti, A., Gérard, J.-C., Jia, X., Nichols, J. D., & Clarke, J. T. (2009). Auroral footprint of Ganymede. *Journal of Geophysical Research*, *114*, A07212. <https://doi.org/10.1029/2009JA014289>
- Gurnett, D. A., & Goertz, C. K. (1981). Multiple Alfvén wave reflections excited by Io origin of the Jovian decametric arcs. *Journal of Geophysical Research*, *86*, 717–722.
- Gustin, J., Gérard, J.-C., Grodent, D., Gladstone, G. R., Clarke, J. T., Pryor, W. R., et al. (2013). Effects of methane on giant planet's UV emissions and implications for the auroral characteristics. *Journal of Molecular Spectroscopy*, *291*, 108–117.
- Hess, S. L. G., Bonfond, B., Chantry, V., Gérard, J.-C., Grodent, D., Jacobsen, S., & Radioti, A. (2013). Evolution of the Io footprint brightness II: Modeling. *Planetary Space Science*, *88*, 76–85.
- Hess, S. L. G., Delamere, P., Dols, V., Bonfond, B., & Swift, D. (2010). Power transmission and particle acceleration along the Io flux tube. *Journal of Geophysical Research*, *115*, A06205. <https://doi.org/10.1029/2009JA014928>
- Hinton, P. C., Bagenal, F., & Bonfond, B. (2019). Alfvén wave propagation in the Io plasma torus. *Geophysical Research Letters*, *46*, 1242–1249. <https://doi.org/10.1029/2018GL081472>
- Hue, V., Gladstone, G. R., Greathouse, T. K., Kammer, J. A., Davis, M. W., Bonfond, B., et al. (2019). In-flight characterization and calibration of the Juno-ultraviolet spectrograph (Juno-UVS). *The Astronomical Journal*, *157*, 90.
- Ip, W.-H., & Goertz, C. K. (1983). An interpretation of the dawn-dusk asymmetry of UV emission from the Io plasma torus. *Nature*, *302*, 232.
- Jacobsen, S., Neubauer, F. M., Saur, J., & Schilling, N. (2007). Io's nonlinear MHD-wave field in the heterogeneous Jovian magnetosphere. *Geophysical Research Letters*, *34*, L10202. <https://doi.org/10.1029/2006GL029187>
- Jessup, K. L., & Spencer, J. R. (2015). Spatially resolved HST/STIS observations of Io's dayside equatorial atmosphere. *Icarus*, *248*, 165–189.
- Jessup, K. L., Spencer, J. R., Ballester, G. E., Howell, R. R., Roesler, F., Vigel, M., & Yelle, R. (2004). The atmospheric signature of Io's Prometheus plume and anti-Jovian hemisphere: Evidence for a sublimation atmosphere. *Icarus*, *169*, 197–215.
- Jia, X., Kivelson, M. G., Khurana, K. K., & Walker, R. J. (2010). Magnetic fields of the satellites of Jupiter and Saturn. *Space Science Reviews*, *152*(1), 271–305. <https://doi.org/10.1007/s11214-009-9507-8>
- Kammer, J. A., Hue, V., Greathouse, T. K., Gladstone, G. R., Davis, M. W., & Versteeg, M. H. (2018). Planning operations in Jupiter's high-radiation environment: optimization strategies from Juno-UVS. Society of photo-optical instrumentation engineers (spie) conference series, vol. 10699, p. 106993A.
- Kivelson, M. G., Bagenal, F., Kurth, W. S., Neubauer, F. M., Paranicas, C., & Saur, J. (2004). Magnetospheric interactions with satellites. In F. Bagenal, T. E. Dowling, & W. B. McKinnon (Eds.), *Jupiter: the planet, satellites and magnetosphere* (pp. 513–536). Cambridge, UK: Cambridge University Press.
- Lellouch, E., Ali-Dib, M., Jessup, K.-L., Smette, A., Käufel, H.-U., & Marchis, F. (2015). Detection and characterization of Io's atmosphere from high-resolution 4- μ m spectroscopy. *Icarus*, *253*, 99–114.
- Lellouch, E., McGrath, M. A., & Jessup, K. L. (2007). Io's atmosphere. In R. M. C. Lopes, & J. R. Spencer (Eds.), *Io after Galileo: A new view of Jupiter's volcanic moon* (pp. 231). Berlin, Heidelberg: Springer Praxis Books / Geophysical Sciences.
- Li, W., Thorne, R. M., Ma, Q., Zhang, X.-J., Gladstone, G. R., Hue, V., et al. (2017). Understanding the origin of Jupiter's diffuse aurora using Juno's first perijove observations. *Geophysical Research Letters*, *44*, 10,162–10,170. <https://doi.org/10.1002/2017GL075545>
- Markwardt, C. B. (2009). Non-linear least-squares fitting in IDL with MPFIT. In D. A. Bohlender, D. Durand, & P. Dowler (Eds.), *Astronomical data analysis software and systems xviii*, Astronomical Society of the Pacific Conference Series (Vol. 411, pp. 251). Maryland: NASA/GSFC.
- McGrath, M. A., Belton, M. J. S., Spencer, J. R., & Sartoretti, P. (2000). Spatially resolved spectroscopy of Io's Pele Plume and SO₂ atmosphere. *Icarus*, *146*, 476–493.
- Morabito, L. A., Synnott, S. P., Kupferman, P. N., & Collins, S. A. (1979). Discovery of currently active extraterrestrial volcanism. *Science*, *204*, 972.

- Mura, A., Adriani, A., Connerney, J. E. P., Bolton, S., Altieri, F., Bagenal, F., et al. (2018). Juno observations of spot structures and a split tail in Io-induced aurorae on Jupiter. *Science*, *361*, 774–777. <https://doi.org/10.1126/science.aat1450>
- Murakami, G., Yoshioka, K., Yamazaki, A., Tsuchiya, F., Kimura, T., Tao, C., et al. (2016). Response of Jupiter's inner magnetosphere to the solar wind derived from extreme ultraviolet monitoring of the Io plasma torus. *Geophysical Research Letters*, *43*, 12,308–12,316. <https://doi.org/10.1002/2016GL071675>
- Neubauer, F. M. (1980). Nonlinear standing Alfvén wave current system at Io—Theory. *Journal of Geophysical Research*, *85*, 1171–1178.
- Neubauer, F. M. (1998). The sub-Alfvénic interaction of the Galilean satellites with the Jovian magnetosphere. *Journal of Geophysical Research*, *103*, 19,843–19,866.
- Peale, S. J., Cassen, P., & Reynolds, R. T. (1979). Melting of Io by tidal dissipation. *Science*, *203*, 892–894.
- Pearl, J., Hanel, R., Kunde, V., Maguire, W., Fox, K., Gupta, S., et al. (1979). Identification of gaseous SO₂ and new upper limits for other gases on Io. *Nature*, *280*, 755–758.
- Radioti, A., Tomás, A. T., Grodent, D., Gérard, J.-C., Gustin, J., Bonfond, B., et al. (2009). Equatorward diffuse auroral emissions at Jupiter: Simultaneous HST and Galileo observations. *Geophysical Research Letters*, *36*, L07101. <https://doi.org/10.1029/2009GL037857>
- Retherford, K. D., Moos, H. W., Strobel, D. F., Wolven, B. C., & Roesler, F. L. (2000). Io's equatorial spots: Morphology of neutral UV emissions. *Journal of Geophysical Research*, *105*, 27,157–27,166.
- Retherford, K. D., Spencer, J. R., Stern, S. A., Saur, J., Strobel, D. F., Steffl, A. J., et al. (2007). Io's atmospheric response to eclipse: UV aurorae observations. *Science*, *318*, 237–240.
- Roesler, F. L., Moos, H. W., Oliverson, R. J., Woodward, R. C., Retherford, K. D., Scherb, F., et al. (1999). Far-ultraviolet imaging spectroscopy of Io's atmosphere with HST/STIS. *Science*, *283*, 353–357.
- Roth, L., Saur, J., Retherford, K. D., Feldman, P. D., & Strobel, D. F. (2014). A phenomenological model of Io's UV aurora based on HST/STIS observations. *Icarus*, *228*, 386–406.
- Roth, L., Saur, J., Retherford, K. D., Strobel, D. F., & Spencer, J. R. (2011). Simulation of Io's auroral emission: Constraints on the atmosphere in eclipse. *Icarus*, *214*, 495–509.
- Sandel, B. R., & Broadfoot, A. L. (1982). Io's hot plasma torus—A synoptic view from Voyager. *Journal of Geophysical Research*, *87*, 212–218.
- Saur, J., Grambusch, T., Duling, S., Neubauer, F. M., & Simon, S. (2013). Magnetic energy fluxes in sub-Alfvénic planet star and moon planet interactions. *Astronomy & Astrophysics*, *552*, A119.
- Saur, J., Neubauer, F. M., Connerney, J. E. P., Zarka, P., & Kivelson, M. G. (2004). Plasma interaction of Io with its plasma torus. In F. Bagenal, T. E. Dowling, & W. B. McKinnon (Eds.), *Jupiter: the planet, satellites and magnetosphere* (Vol. 1, pp. 537–560). Cambridge, UK: Cambridge University Press.
- Saur, J., Neubauer, F. M., Strobel, D. F., & Summers, M. E. (1999). Three-dimensional plasma simulation of Io's interaction with the Io plasma torus: Asymmetric plasma flow. *Journal of Geophysical Research*, *104*, 25,105–25,126.
- Saur, J., Neubauer, F. M., Strobel, D. F., & Summers, M. E. (2000). Io's ultraviolet aurora: Remote sensing of Io's interaction. *Geophysical Research Letters*, *27*, 2893–2896.
- Saur, J., & Strobel, D. F. (2004). Relative contributions of sublimation and volcanoes to Io's atmosphere inferred from its plasma interaction during solar eclipse. *Icarus*, *171*, 411–420.
- Saur, J., Strobel, D. F., Neubauer, F. M., & Summers, M. E. (2003). The ion mass loading rate at Io. *Icarus*, *163*, 456–468.
- Spencer, J. R., Lellouch, E., Richter, M. J., López-Valverde, M. A., Jessup, K. L., Greathouse, T. K., & Flaud, J.-M. (2005). Mid-infrared detection of large longitudinal asymmetries in Io's SO₂ atmosphere. *Icarus*, *176*, 283–304.
- Szalay, J. R., Bonfond, B., Allegrini, F., Bagenal, F., Bolton, S., Clark, G., et al. (2018). In situ observations connected to the Io footprint tail aurora. *Journal of Geophysical Research: Planets*, *123*, 3061–3077. <https://doi.org/10.1029/2018JE005752>
- Thomas, N., Bagenal, F., Hill, T. W., & Wilson, J. K. (2004). The Io neutral clouds and plasma torus. In F. Bagenal, T. E. Dowling, & W. B. McKinnon (Eds.), *Jupiter: the planet, satellites and magnetosphere* (Vol. 1, pp. 561–591). Cambridge, UK: Cambridge University Press.
- Trafton, L. M., Moore, C. H., Goldstein, D. B., Varghese, P. L., & McGrath, M. A. (2012). HST/STIS observations and simulation of Io's emission spectrum in Jupiter shadow: Probing Io's Jupiter-facing eclipse atmosphere. *Icarus*, *220*, 1121–1140.
- Tsang, C. C. C., Spencer, J. R., & Jessup, K. L. (2015). Non-detection of post-eclipse changes in Io's Jupiter-facing atmosphere: Evidence for volcanic support? *Icarus*, *248*, 243–253.
- Tsang, C. C. C., Spencer, J. R., Lellouch, E., Lopez-Valverde, M. A., & Richter, M. J. (2016). The collapse of Io's primary atmosphere in Jupiter eclipse. *Journal of Geophysical Research: Planets*, *121*, 1400–1410. <https://doi.org/10.1002/2016JE005025>
- Tsang, C. C. C., Spencer, J. R., Lellouch, E., López-Valverde, M. A., Richter, M. J., & Greathouse, T. K. (2012). Io's atmosphere: Constraints on sublimation support from density variations on seasonal timescales using NASA IRTF/TEXES observations from 2001 to 2010. *Icarus*, *217*, 277–296.
- Wannawichian, S., Clarke, J. T., Bagenal, F., Smyth, W. H., Peterson, C. A., & Nichols, J. D. (2013). Longitudinal modulation of the brightness of Io's auroral footprint emission: Comparison with models. *Journal of Geophysical Research: Space Physics*, *118*, 3336–3345. <https://doi.org/10.1002/jgra.50346>
- Wannawichian, S., Clarke, J. T., & Nichols, J. D. (2010). Ten years of Hubble Space Telescope observations of the variation of the Jovian satellites' auroral footprint brightness. *Journal of Geophysical Research*, *115*, A02206. <https://doi.org/10.1029/2009JA014456>